Soft X-Ray Emission from Saturn's Magnetosheath II: Solar Wind Driving

D. Naylor[1], L. C. Ray[1], P. C. Rogan[12], W. R. Dunn[3], H. T. Smith[4]

[1]Space and Planetary Physics Group, Department of Physics, Lancaster University, Lancaster, UK
[2]Institute of Geophysics and Meteorology, University of Cologne, Cologne, DE
[3]Department of Physics & Astronomy, University College London, London, UK
[4]Space Physics Group, Space Exploration Sector, Johns Hopkins University Applied Physics Laboratory, Laurel, MD, USA

Key Points:

- Modelled soft X-ray emission at Saturn's magnetosheath is presented with rates on the order 10^{-10}-10^{-11} photon cm^{-3} s^{-1}.
- Emission is higher for fast solar wind as a compressed magnetosphere has higher neutral density in the magnetosheath.
- A SMILE-like instrument can detect around 100 photons in a quarter of a planetary rotation but detector improvements obtain up to thousands.

Corresponding author: Dan Naylor, d.naylor@lancaster.ac.uk

Abstract

Saturn's magnetosphere is dominated by Enceladus-sourced neutrals, which spread throughout the system into the magnetosheath. The neutrals can charge exchange with highly charged solar wind ions, causing soft X-ray emission (< 2 keV) upon de-excitation of the ion. Imaging these soft X-rays can reveal the global, dynamic structure of the magnetosheath and cusps of a magnetosphere and give insight into the complex nature of the solar wind interaction with the planet. A model of soft X-ray emission from Saturn's magnetosheath is presented, considering charge exchange between Enceladus-sourced neutrals and highly charged oxygen ions (O^{7+} and O^{8+}). We estimate emission rates and the flux that would be detected by a SMILE-like soft X-ray imager (SXI). Solar wind dynamic pressure is varied to test the effect of solar wind conditions on X-ray production. Volumetric emission rate is on the order of 10^{-11} and 10^{-10} photon cm^{-3} s^{-1} for slow and fast solar winds, respectively. A compressed magnetosphere has higher neutral density in the magnetosheath leading to more emission. For a SMILE-like SXI imaging at at a distance of 53 R_S, we estimate over a hundred photons can be detected within a quarter of a planetary rotation. A 'future' SXI, with double the FOV of SMILE's and 100 cm^2 effective area, significantly improves integration times, reducing integration time to ~ 2.5 s when imaging at 25 R_S. Under a point source approximation, the modelled SXIs perform well to large distances, with Earth-based observations potentially being possible with an XMM-Newton-like instrument.

Plain Language Summary

Saturn's magnetosphere is filled with neutral particles, mostly ejected from the icy moon Enceladus. These particles spread throughout the system and into the magnetosheath, the region just outside the magnetosphere which contains slowed, heated solar wind (the continuous stream of particles sourced from the Sun). Inside the magnetosheath, solar wind particles can interact with neutrals through a process known as charge exchange, leading to the emission of soft X-rays. These can be imaged by a soft X-ray imager (SXI), and allow for a global, moving view of the magnetosheath to be built, giving insight into how the solar wind effects the magnetosphere. A new model is presented to test emission rates for different solar wind conditions. Using a SMILE-like SXI, the instrument images a hundred photons in a quarter of a Saturnian rotation. By improving the specifications of the SXI to test a future imager, integration times are reduced to under one minute, allowing rapid imaging. When the SXI is moved back from the system and all incoming flux is summed, Earth-based imaging may be possible with an XMM-Newton-like instrument.

1 Introduction

It has long been known that neutral particles are present within Saturn's magnetosphere, with atomic hydrogen first discovered reported by Weiser et al. (1977). After the Voyager 1 and 2 flybys an extended hydrogen cloud (Shemansky & Hall, 1992), as well as a hydroxyl (OH) cloud (Shemansky et al., 1993) were discovered, revealing the magnetosphere to be neutral-dominated rather than plasma-dominated (Richardson et al., 1998). The arrival of the Cassini-Huygens mission further enriched understanding of the neutrals at Saturn, with the UVIS instrument discovering an oxygen cloud (Esposito et al., 2005). These neutrals are distributed throughout the system (Melin et al., 2009), being predominantly sourced from the cryovolcanic moon Enceladus (e.g. Porco et al. (2006); Spencer et al. (2006)) which ejects ice into the magnetosphere at a rate of ~ 280 kg s^{-1} (H. T. Smith & Richardson, 2021). This water forms a dense torus centred on Enceladus's orbit. The H_2O undergoes photodissociation and is broken down into H, O, and OH. Neutral-neutral collisions and other processes redistribute the particles into tori

(Jurac and Richardson (2005) Johnson et al. (2006)) which extend throughout the magnetosphere, into the magnetosheath region and beyond (H. T. Smith & Richardson, 2021).

Over 13 years, Cassini, with a wealth of crossing data, characterised the magnetopause and bow shock regions. The typical standoff distances of the two are between 18 and 25 R_S and 20 and 40 R_S, respectively (Jackman et al., 2019) ($R_S = 60268$ km, Saturn radius). Both internal plasma and the solar wind have an effect on Saturn's magnetospheric dynamics due to the rapid rotation of the planet and magnetosphere, but the extent to which both have control has been long debated (Masters et al., 2014). The solar wind impinges on the magnetosphere with a dynamic pressure given by $P_{\mathrm{dyn}} = n_p m_p v_{\mathrm{SW}}^2$, where n_p is the proton number density of the solar wind, m_p is the proton mass and v_{SW} is the solar wind speed. Compression of the magnetosphere by solar wind enhancements has been established as an important trigger of magnetospheric dynamics (Bunce et al., 2005), and spacecraft observations have observed reconnection occurring at the magnetopause (Huddleston et al., 1997), but is is not known whether reconnection alone can drive the dynamics of the system. On the other hand,Pilkington et al. (2015) concluded that internal, hot plasma dynamics can take almost complete control of the magnetosphere's dayside size and shape, causing movement of the magnetopause by up to 15 R_S at constant solar wind conditions. Clearly, Saturn's system is not static, and the balance between internal plasma and solar wind driving is far from completely understood (Mo et al., 2023).

X-rays from Saturn have been unambiguously observed by Earth-orbiting observatories several times (e.g. J.-U. Ness, Schmitt, Wolk, et al. (2004); J.-U. Ness, Schmitt, and Robrade (2004)). Emission is largely caused by scattering of solar X-rays, from the planetary disk (Bhardwaj et al., 2005; Cravens et al., 2006) and from atomic oxygen in icy ring material, driving fluorescent emission centred on 0.53 keV. X-ray aurora (e.g. Cravens et al. (1995a)) was expected at Saturn, but has yet to be observed (Branduardi-Raymont et al., 2010, 2013; Hui et al., 2010). Within the magnetosheath, heavily stripped solar wind ions such as O^{7+} and O^{8+} can interact with magnetospheric neutrals through charge exchange (Connor et al., 2021), in which the ion acquires an electron from the neutral. When the partially neutralised ion, O^{6+*}, de-excites, photons in the soft X-ray (< 2 keV) range are emitted (Ng et al., 2023). A mission has not yet focussed on magnetosheath-sourced X-rays at Saturn, hence they have not yet been detected.

Soft X-ray imagers (SXIs) can be used as a diagnostic tool for the plasma structures of regions such as the magnetosheath and cusps. With the changing state of the magnetopause and bow shock driven by solar wind variations and internal plasma, a dynamic image of the magnetosheath can be built in soft X-rays. This, in turn, allows the exploration of the extent to which the solar wind drives magnetospheric dynamics (Sibeck et al., 2018). The dominant driver of Saturn's magnetospheric dynamics is still debated long after the end of the Cassini mission, so soft X-ray imaging may provide a novel method of exploring the system to answer the question to this mystery. While Cassini data revealed much information about the magnetopause and bow shock, allowing models of the surfaces to be built (e.g. Kanani et al. (2010); Pilkington et al. (2015); Went et al. (2011)), these measurements were in-situ and relied on a single spacecraft crossing the boundaries. Soft X-ray images present a more global view of the magnetosheath region, revealing insights into the movement and structure of the boundaries as a whole.

Soft X-rays have been discovered across the solar system, including at comets (Lisse et al., 1996) and Jupiter's aurora (Dunn et al., 2022), but magnetosheath-generated soft X-ray emission has been scarcely explored apart from Earth-based missions. Therefore, the field of soft X-ray imaging is still emerging as a new tool to deepen our understanding of planetary magnetospheres. In 2025, the European Space Agency (ESA) and the Chinese Academy of Sciences (CAS) will launch SMILE (Solar Wind-Magnetosphere-Ionosphere Link Explorer), which will have an SXI onboard to detect soft X-rays from Earth's magnetosheath region. SMILE's SXI is the cutting edge of SXI technology, with

a wide field-of-view (FOV) detector (Sembay et al., 2024). Leppard et al. (2025) modelled soft X-ray emission rates from the Jovian magnetosheath and found that they are unlikely to be distinguishable from the soft X-ray background due to the large system scales and low neutral density within the magnetosheath. However, due to the dominance of the neutral clouds at Saturn and the smaller scale of the magnetosheath, the case for X-ray imaging may be more positive.

Rogan et al. (submitted) uses MHD simulation data to characterise soft X-ray emission from Saturn's magnetosheath. We present a simple 3D model to explore how changes in solar wind speed, dynamic pressure and composition affect X-ray emission rates. Solar wind dynamic pressure changes can be rapid (e.g. Thomsen et al. (2019)), so it is important to explore whether imaging is possible within reasonable timescales, otherwise any changes driven by the solar wind variations would be missed by the imager. Therefore we estimate the rate of flux detection by an SXI on approach to Saturn along the planet-Sun line, translating this to minimum integration times. Section 2 of this study details the model used and section 3 reports and discusses the results gained for various solar wind conditions as well as soft X-ray imager configurations.

2 The Model

This models uses the Kronocentric Solar Magnetospheric (KSM) coordinate system, where the x-axis is along the Saturn-Sun line, the y-z plane contains the planet's centered dipole axis, and the z-axis completes the right hand set (Fuselier et al., 2020).

2.1 Neutral Cloud Densities

Neutral tori are constructed from the work of H. T. Smith and Richardson (2021), which provides spatial distributions of Enceladus-sourced H, O and OH in Saturn's magnetosphere to 20 R_S, constrained by Cassini data. We extend the tori to 50 R_S and ignore the source region (inside 10 R_S) in order to focus on the magnetosheath. Scale heights are incorporated in the z-direction, constraining the neutral tori to the equatorial plane. The radial profiles of the neutral tori are

$$n_n = a_n \exp(-b_n r) \exp\left(\frac{-z}{f_{\text{scale}_n}}\right) \tag{1}$$

where f_{scale_n} is a species-dependent scale height function, logarithmic for H, quadratic for OH and approximated as 1 for O.

$$f_{\text{scale,H}} = a_{\text{scale}} \ln(b_{\text{scale}} r) + c_{\text{scale}} \tag{2}$$

$$f_{\text{scale,O}} = a_{\text{scale}} r^2 + b_{\text{scale}} r + c \tag{3}$$

The neutral tori are presented in figure 1 while the parameters for the profiles and scale heights are given in table 1.

2.2 Magnetopause and Bow Shock Surfaces

The shape of the magnetopause is given by the model of Kanani et al. (2010)

$$R_{\text{MP}} = R_0 \left(\frac{2}{1+\cos\theta}\right)^K \tag{4}$$

where R_{MP} is the position of the magnetopause point (R_S), R_0 is the subsolar stand off distance, θ is the polar angle, and K is the flaring parameter of the magnetopause. Pa-

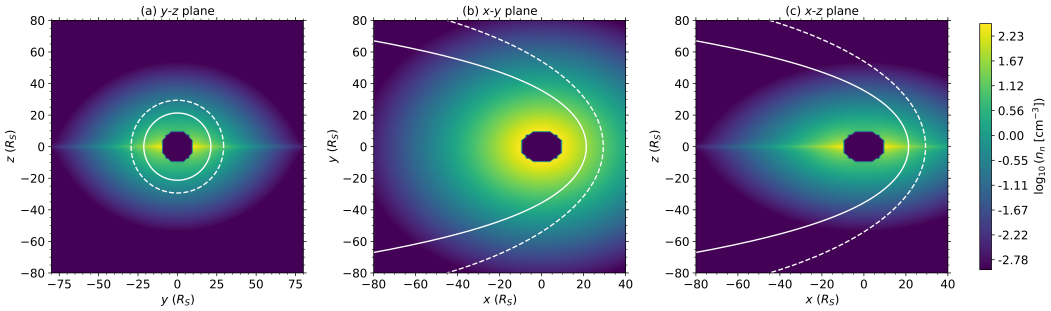

Figure 1. Enceladus-sourced neutral particle densities outside of 10 R_S. (a), (b) and (c) show the tori in the y-z, x-y and x-z planes respectively. Scale heights act in the z-direction meaning the tori are confined within the equatorial plane. The magnetopause and bow shock surfaces are shown by grey lines (bow shock is dotted).

Cloud	$a \times 10^2$	$b \times 10^{-1}$	a_{scale}	b_{scale}	c_{scale}
O	9.57	1.69	-	-	-
H	5.46	1.66	5.55	0.546	-6.02
OH	2.80	1.98	0.0016	0.0712	1.070

Table 1. Enceladus-sourced neutral tori density profiles, fit to $n = a\exp(-bx)\exp(-z/f_{\text{scale}})$, and species-dependent scale heights which define the scale height function f_{scale}. For H, the scale height equation is logarithmic, for OH, quadratic, and approximated as 1 for O.

rameters are defined such that

$$R_0 = a_1 P_{\text{dyn}}^{-a_2} \tag{5}$$

$$K = a_3 + a_4 P_{\text{dyn}} \tag{6}$$

where P_{dyn} is the solar wind dynamic pressure in nPa, $a_1 = 10.3$, $a_2 = 0.20$ and $a_3 = 0.73$.

Saturn's magnetopause exhibits significant polar flattening (∼19%) due to the rapid rotation of the planet confining magnetospheric plasma close to the equatorial plane (Pilkington et al., 2014). The Kanani et al. (2010) magnetopause model does not incorporate this flattening, but since soft X-ray emission is expected to be strongest near the equatorial plane where neutral density is highest, it is sufficient for our analysis.

The bow shock surface is defined by the semi-empirical model of Went et al. (2011)

$$R_{\text{BS}} = \frac{(1+\epsilon)c_1 P_{\text{dyn}}^{-1/c_2}}{1+\epsilon\cos\theta} \tag{7}$$

where R_{BS} is the radial distance from Saturn to a point on the bow shock, again in R_S, θ is the polar angle between the point on the bow shock surface and the Saturn-Sun line, and ϵ is the eccentricity of the shock (describing how blunt or streamlined it is). The parameters are given as $\epsilon = 0.84$, $c_1 = 15$ R_S and $c_2 = 5.4$ R_S.

An extensive survey of Saturn's magnetosheath properties from Cassini data was conducted by Sergis et al. (2013), who examined plasma, magnetic field and particle measurements made by the suite of instruments onboard Cassini. They reported an ion density varying between 0.05 and 0.25 cm^{-3}, with protons contributing ∼ 95% of the total ion composition. The average number density of plasma within the sheath was 0.1

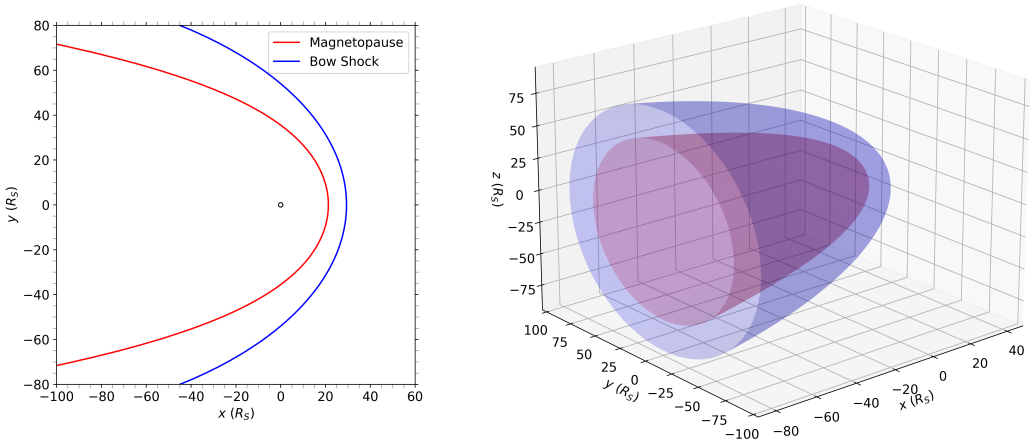

Figure 2. Magnetopause (red) and bow shock (blue) surfaces of Kanani et al. (2010) and Went et al. (2011) respectively, shown in both the x-y plane and in 3D. Here, $P_{\rm dyn} = 0.02656$ nPa meaning standoff distances are 21 R_S and ∼29 R_S for the magnetopause and bow shock, respectively.

cm^{-3}. Furthermore, they found ion temperatures to be between 210 and 370 eV - this was refined in a later analysis by Shen et al. (2022), who reported an average ion temperature of 304 eV. The magnetosheath density and temperature is fixed at the average value of 0.1 cm^{-3} and 304 eV ($\sim 3.5 \times 10^6$ K) respectively. Bulk ion speed is also approximated to be constant throughout the magnetosheath, at the solar wind speed.

2.3 Soft X-Ray Emission Rate

The volumetric emission of soft X-rays due to charge exchange is given by

$$P = \sum_n n_n n_q v_{\rm rel} \sigma_{sqn} b_{sqj} \tag{8}$$

where n_n is neutral density (with the summation over n reflecting the multiple neutral species present), n_q is solar wind ion density, $v_{\rm rel}$ is the relative velocity between the ion and neutral particle, σ_{sqn} is a cross section of the interaction and b_{sqj} is the branching ratio (see Whittaker et al. (2016) and Sibeck et al. (2018)).

Relative velocity is given by

$$v_{\rm rel} \sim \left(v_{\rm bulk}^2 + v_{\rm therm}^2\right)^{1/2} \tag{9}$$

where $v_{\rm bulk}$ is approximated in this model as $v_{\rm SW}$ and taken as constant over the whole magnetosheath region. $v_{\rm therm}$ is given by

$$v_{\rm therm} = \sqrt{\frac{3 k_B T}{m_p}} \tag{10}$$

where k_B is the Boltzmann constant, T is the ion temperature of the solar wind (304 eV (see section 2.2)), and m_p is the proton mass. In this study, we consider only charge exchange between neutrals and highly-charged oxygen ions (O^{7+} and O^{8+}). Hence, n_q is the O^{7+} or O^{8+} density within the magnetosheath, which will charge exchange with the neutrals. Whittaker and Sembay (2016) used thirteen years of Advanced Composition

Explorer (ACE) data to characterise highly-charged oxygen abundances within the solar wind. They provide equations

$$\mathrm{O^{7+}/O} = 28120 \times v_{\mathrm{SW}}^{-2.077} \tag{11}$$

$$\mathrm{O^{8+}/O} = 0.274 \times \left(\mathrm{O^{7+}/O}\right)^{1.951} \tag{12}$$

$$\mathrm{O/H} = (-3.16 \times 10^{-4}) + (1.83 \times 10^{-6}) v_{\mathrm{SW}} - (9.45 \times 10^{-10}) v_{\mathrm{SW}}^2 \tag{13}$$

which allows the solar wind velocity-dependent abundances of $\mathrm{O^{7+}}$ and $\mathrm{O^{8+}}$ to be determined.

The charge exchange interaction cross sections used in this study are from Bodewits et al. (2007), who provide values for interactions between $\mathrm{O^{7+}/O^{8+}}$ and hydrogen-like neutrals, and Schwadron and Cravens (2000), who provide them for oxygen-like neutrals. OH is taken to have O-like cross sections due to oxygen's cross section being significantly higher than hydrogen's. From Bodewits et al. (2007), cross sections are summed at 400 km $\mathrm{s^{-1}}$ and 600 km $\mathrm{s^{-1}}$, taken to be 58.45×10^{-16} $\mathrm{cm^{-2}}$ and 57.26×10^{-16} $\mathrm{cm^{-2}}$ respectively. For oxygen, the constant cross section of 12×10^{-15} $\mathrm{cm^{-2}}$ is used. The cross sections from Bodewits et al. (2007) are wrapped into the b_{sqj} term and the same is approximated for the oxygen cross sections.

2.4 Intensity, Flux and Integration Time

SXI properties ultimately determine whether soft X-ray emission from the magnetosheath can be detected. The incident flux on an SXI instrument is dependent on the distance of the imager from the system as well as the effective area of the detector. The SXI viewing geometry is considered on approach to the system side-on (to allow for an equatorial orbit, and avoid reflected emission from the disk of the planet). The minimum approach distance of the SXI required to image the system area considered in the model is given by

$$d_y = \frac{50\ R_S}{\tan\left(\mathrm{FOV_{SXI}}/2\right)} \tag{14}$$

where 50 R_S is half of our modelled domain when viewed from dawn. The total minimum approach distance is given by

$$d_{\mathrm{approach}} = \sqrt{\left(d_y - y\right)^2 + x^2 + z^2} \tag{15}$$

The intensity of soft X-ray emissions along a line of sight is

$$I = \int P dl \frac{d\Omega}{4\pi} = \frac{1}{2} \int P dy \tag{16}$$

where P is the volumetric emission, dl is the line element along the line of sight of the SXI, taken here as dy, and $d\Omega$ is the solid angle increment. Only forward propagated emission is being considered, hence the solid angle integrates to 2π. The intensity is then scaled from a box of area 1 R_S^2 to the distance of the SXI by a factor of $1/d_{\mathrm{approach}}^2$ to calculate flux detected by the SXI. Multiplying flux by the effective area of the SXI, A_{eff}, gives count rate in $\mathrm{s^{-1}}$. The inverse of the maximum count rate gives the minimum integration time, the time required to image one photon, in seconds.

The count rate per-pixel (Gustin et al., 2012) is expressed as

$$C_{\mathrm{pixel}} = A \int I_\lambda Q_\lambda T_\lambda m_x m_y d\lambda \tag{17}$$

$$\approx A_{\mathrm{eff}} I m_x m_y \tag{18}$$

$$= C_{\mathrm{detector}} m_x m_y \tag{19}$$

where A is the area of the detector, I_λ is the surface brightness of the source in photon cm^{-2} s^{-1} Å^{-1} arcsecond^{-1}, Q_λ is the instrument sensitivity and T_λ is the filter transmission. This means $Q_\lambda T_\lambda$ is the probability of detecting a count per incident photon. C_{detector} is the count rate for the whole detector. Finally, m_x and m_y are the plate scales of a pixel along the x and y axes respectively. In the approximation, I is the flux detected by the whole SXI. From the specifications of SMILE from Sembay et al. (2024), there are two CCDs with 4510×4510 pixels, $m_x m_y = 3.08 \times 10^{-9}$ sr, so

$$C_{\text{pixel}} = C_{\text{detector}} \times (3.09 \times 10^{-9}) \tag{20}$$

Clearly, per-pixel integration times will be significantly higher than for the whole detector.

Two SXIs are considered, firstly a SMILE-like imager, then a simple 'future SXI' concept is explored, with double the FOV of SMILE and an effective area of 100 cm^2. The increased FOV reduces the minimum distance at which the SXI must be from the system such that it can image the whole dayside magnetosheath, while the increased effective area doubles the count rate of the detector. Overall, the improvements serve to reduce integration times significantly. While this may be an ambitious SXI configuration, the LEXI SXI (Lunar Environment Heliophysics X-ray Imager) has an effective area of 44 cm^2 (Walsh et al., 2024) and the BepiColobo X-ray imager, MIXS, is ready to image Mercury (Fraser et al., 2010), so 100 cm^2 in the future is not out of the realm of possibility. That said, there is a trade-off between FOV and effective area, so consideration should be given to the realistic limits of what could be expected for an SXI. The configurations and minimum imaging distance of the two SXIs are reported in table 2, with SMILE's being given by Sembay et al. (2024).

SXI	FOV	A_{eff} (cm^2)	d_{approach} (R_S)
SMILE	$26.5° \times 15.5°$	9.6	212
Future	$53° \times 31°$	19.2	100

Table 2. FOV, effective area (A_{eff}) and minimum imaging distance (d_{approach}) for the SMILE (see Sembay et al. (2024)) and future SXIs, where the future imager is a hypothetical instrument for a outer planetary mission with double the FOV and effective area of SMILE.

3 Results and Discussion

3.1 Full Magnetosheath Imaging

We first consider a SMILE-like SXI placed at an imaging distance of 212 R_S such that it can capture the full dayside magnetosheath. We impose solar wind with $v_{\text{SW}} =$ 400 km s^{-1} and $P_{\text{dyn}} = 0.02656$ nPa. Figure 3 shows volumetric emission rate and intensity in the y-z, x-y and x-z planes. Emission is most strongly concentrated at the nose of the magnetopause, where neutral density is highest. In the x-y plane, the emission rate extends moving dawn- and dusk-ward through the magnetosheath, decreasing with the neutral density. In the y-z and x-z planes, emission is confined to the equatorial region, consistent with the spatial distribution of the neutral tori. The emission rate is strongly dictated by neutral density and opens the possibility of using soft X-ray imaging to track the distribution of neutral particles within planetary magnetosheaths, along with magnetopause and cusp structure and location.

Figure 3(d)-(f) show the modelled flux images obtained by a SMILE-like SXI on approach to Saturn. Looking towards the nose of the magnetopause, there is a clear sig-

nature of emission. Due to the concentration of emission in the equatorial plane, the modelled flux shows the nose of the magnetopause very clearly, rapidly dropping in intensity in the z-direction. The flank view similarly shows the concentration of emission to the equatorial plane. Circular striations within the flux image are a numerical artefact due to the grid spacing and discrete steps in the magnetopause boundary. Since Saturn is an efficient reflector of solar X-rays (Bhardwaj et al., 2005), all flux measurements are considered from the side-on perspective to avoid contamination from the disk of the planet. We report the number of photons imaged within a quarter of a planetary rotation, $N_{1/4}$ - while detailed analysis of imaging capabilities is not considered in this model, this figure provides a simple measure of whether imaging may be reasonable within system timescales.

The maximum volumetric emission rate and flux are calculated to be 5.56×10^{-11} photon cm^{-3} s^{-1} and 1.02×10^{-4} photon cm^{-2} s^{-1}, respectively, corresponding to an integration time of 0.282 h. This means $N_{1/4} = 9$, i.e. 9 photons can be detected within a quarter of a planetary rotation. This is likely not enough photon detection for imaging to be viable to investigate magnetospheric dynamics. Since SMILE was designed to image Earth's magnetosheath, it is expected that count rates are too low when focussing on the entire sheath region at Saturn. Therefore, modifications must be made to the imaging method in order to improve integration times, either by moving the SXI closer or by using a different SXI with improved configurations.

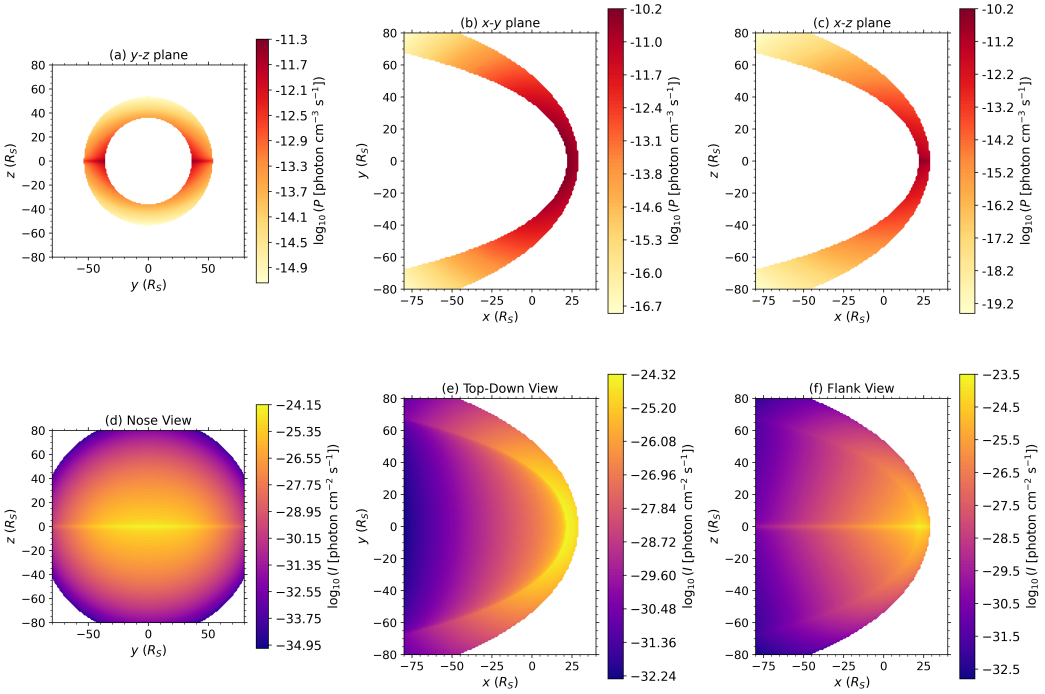

Figure 3. Volumetric emission rate, highlighting the regions of the magnetosheath where emission is strong. Emission is seen in the (a) y-z, (b) x-y and (c) x-z planes, for the slow solar wind case ($v_{\rm SW}$ = 400 km s^{-1}, $P_{\rm dyn}$ = 0.02656 nPa). (d)-(f) show the intensity of the emissions which is scaled to a flux at the SXI on approach to Saturn.

3.2 SXI Modifications

The results tested in section 3.1 with a SMILE-like SXI give integration times lower than a planetary rotation and other system timescales. However at ∼15 minutes/photon,

imaging is likely infeasible. Solar wind variations can be rapid and changes in emission driven by these short timescale changes may be missed with the SMILE-like SXI imaging the whole magnetosheath. Therefore, we consider modifications to the SXI or imaging method in order to obtain shorter, more favourable integration times. Table 2 reports flux and corresponding integration times for the different SXI modifications, as well as the imaging distance of the detector configuration.

First tested is the SMILE-like SXI imaging at a closer approach distance, such that it images 1/4 of the magnetosheath (so is imaging at 1/4 of the distance). A future mission may use a spinning spacecraft that is able to scan across the magnetosheath in order for this distance to be viable for imaging. Figure 3 shows that flux, when viewing the system side-on, is most intensely detected from the nose of the magnetopause. Much of the modelled flux image in figure 3 is empty space. Therefore, by imaging closer to the system, flux loss is reduced, and the image is more targeted to emitting areas. Under the slow solar wind case, imaging at a quarter of the full distance (50 R_S) with the SMILE SXI increases flux to peak at 1.37×10^{-3} photon cm^{-2} s^{-1}, corresponding to a minimum integration time of 0.00212 h = 76.3 s. This is shorter by a factor of ~ 16 when compared to imaging the whole system - as expected, when the imaging distance doubles, flux loss increases by a factor of four due to the inverse square law. This improvement allows significantly more photons to be detected within a planetary rotation. Given the better integration times, this method would refine the flux images obtained and expand the usefulness of the SXI in measuring system dynamics. So in summary, a more targeted imaging of the sheath is advised, allowing the current generation of instrumentation to be viable at the Saturnian system.

Under slow wind conditions, the future SXI, with an extended FOV (positioned at 100 R_S), detects a maximum flux of $4.38{\times}10^{-4}$ photon cm^{-2} s^{-1}, meaning a photon can be imaged within 6.33×10^{-3} h $\sim$ 23 s. Again, this is an improvement from results reported in section 3.3, and a further improvement from closer imaging with SMILE - even though the flux detection is lower, the higher effective area dominates and reduces integration times. Many photons would be detected within system timescales (with 420 being imaged within a quarter of a planetary rotation) which may allow for a dynamic picture to be built up showing the different drivers of X-ray emission in the system. This perhaps best highlights the benefits of continuous improvement to the technology deployed on space missions. By combining the future SXI with imaging at a closer distance (25 R_S), integration time is again reduced to $7.28{\times}10^{-4}$ h/photon $\sim$ 2.5 s/photon, allowing $\sim$ 3659 photons to be imaged with a quarter of a planetary rotation. Continuous and fast imaging of photons as allowed by the future and combined SXIs would allow investigation into the rapid solar wind variations. A spacecraft could potentially be moved even closer to the system and image the magnetosheath in more scans, unlocking more possibilities for X-ray investigations. We consider imaging directly side-on to the system. In reality, spacecraft trajectories are complicated - it would be important to examine the orbital positions and apokrones that would likely lead to optimal imaging possibilities.

3.3 Solar Wind Conditions

We now explore how soft X-ray emission rate varies between different solar wind conditions. For all variations we consider, the flux is that measured by the SMILE-like SXI at 53 R_S, to reflect current generation technology. Two cases of solar wind speed and dynamic pressure are considered, along with the baseline case:

1. SMILE at 53 R_S, slow solar wind: $v_{\rm SW} = 400$ km s^{-1}, $P_{\rm dyn} = 0.02656$ nPa
2. Fast solar wind: $v_{\rm SW} = 650$ km s^{-1}, $P_{\rm dyn} = 0.07014$ nPa
3. mSWIM solar wind: $v_{\rm SW} = 500$ km s^{-1}, $P_{\rm dyn} = 0.008$ nPa

Configuration	d_{approach} (R_S)	F (photon cm^{-2} s^{-1})	τ_{int} (h)	$N_{1/4}$
Closer SMILE	53	1.37×10^{-3}	0.0212	125
Future SXI	100	4.43×10^{-4}	0.00633	420
Closer Future	25	3.81×10^{-3}	7.28×10^{-4}	3659

Table 3. Imaging distance (d_{approach}), flux (F_{max}), integration time ($\tau_{\text{int,min}}$) and number of photons imaged within a quarter of a planetary rotation ($N_{1/4}$) for the three tested SXI configuration modifications, including the SMILE-like SXI imaging only a quarter of the magnetosheath at a time such that it can begin imaging at a closer distance from the system, reducing flux loss. Also tested are a future SXI with double the FOV and effective area of SMILE's, and then a combination of the two improvements.

where case 3 is a sample taken from the results of Thomsen et al. (2019) who used the mSWIM solar wind propagation model of Zieger and Hansen (2008) to investigate Saturn's magnetosheath conditions. Note that case 1 is identical to the closer SMILE configuration in section 3.2, results are restated to allow comparison between the different solar wind conditions.

Volumetric emission rates and the flux incident on the closer (53 R_S) SMILE-like SXI are presented in table 4. The first case restates the slow solar wind results for ease of comparison with the solar wind variations. In case 2, volumetric emission rate and flux are 1.05×10^{-10} photon cm^{-3} s^{-1} and 2.67×10^{-3} photon cm^{-2} s^{-1}, respectively. Integration time in this case is 0.0109 h $\sim$ 40 s, allowing 244 photons to be detected with a quarter of a planetary rotation. Emission rates are higher under fast solar wind conditions due to the increased solar wind dynamic pressure impinging on the magnetopause. This compression moves the magnetosheath inwards to a region of higher neutral density and therefore leads to enhanced emission. The neutral density increase, combined with the higher bulk speed of ions in the magnetosheath, offsets the decrease in emission caused by the lower abundance of oxygen under fast wind conditions. We approximate the magnetosheath velocity as constant, focusing on large-scale global changes related to solar wind conditions. However, a model of soft X-ray emission calculated using magnetosheath data from MHD output (Jia et al., 2012) obtains similar volumetric emission rates (Rogan et al., submitted).

In case 3, maximum emission rate is 2.34×10^{-11} photon cm^{-3} s^{-1}, corresponding to a maximum flux of 5.57×10^{-4} photon cm^{-2} s^{-1} and a minimum integration time of 0.052 h, meaning $N_{1/4}$ is 51. The lower dynamic pressure in this case leads to an expanded magnetosphere, meaning that neutral density in the magnetosheath and hence emission are subsequently reduced. The maximum emission rate is just below 1/2 of that seen in the slow wind case, and correspondingly, an integration time over double the previous cases. It is important to note that with a solar wind velocity of $v_{\text{SW}} = 500$ km s^{-1}. Better determination of the heavy ion abundance in the solar wind would serve to improve understanding of the driving of soft X-ray emission. The work of Nitti et al. (2024) has shown that X-ray telescopes (namely XMM-Newton) can be used to better understand the elemental composition of the solar wind. The technique, however, would only be useful when the line of sight of the SXI traverses the magnetosheath, and the information provided when using XMM-Newton is limited due to the spectral resolution of the telescope (Nitti et al., 2024). However, if an SXI could be designed with this technique in mind, higher resolutions may be possible. Overall, techniques to better understand the solar wind abundance through the use of an SXI may be useful to deepen our

understanding of the solar wind and charge exchange processes occurring at outer planetary systems.

Case	v_{SW} (km s^{-1})	P_{dyn} (nPa)	P (photon cm^{-3} s^{-1})	F (photon cm^{-2} s^{-1})	τ_{int} (h)	$N_{1/4}$
1	400	0.02656	5.56×10^{-11}	1.02×10^{-4}	0.0212	125
2	650	0.07014	1.05×10^{-10}	2.67×10^{-3}	0.0109	244
3	500	0.008	2.34×10^{-11}	5.57×10^{-4}	0.052	51

Table 4. Volumetric emission rate (P) and flux (F) detected by a SMILE-like SXI imaging at 53 R_S side-on to Saturn for three different cases, representing the magnetosphere under different solar wind conditions. This includes slow solar wind ($v_{\mathrm{SW}} = 400$ km s^{-1}, $P_{\mathrm{dyn}} = 0.02656$ nPa), fast wind ($v_{\mathrm{SW}} = 650$ km s^{-1}, $P_{\mathrm{dyn}} = 0.07014$ nPa) and a sample of data from the mSWIM solar wind propagation model ($v_{\mathrm{SW}} = 500$ km s^{-1}, $P_{\mathrm{dyn}} = 0.008$ nPa).

All previous results have stated the time required for the whole detector to image photons. In order to generate a full image, the integration time per pixel must be considered (see section 2.4. Unfortunately, integration times per pixel are on the order of 10^7 h, clearly far too high for any imaging to take place. Even under a point source approximation (which may be valid at a far enough approach distance), the times remain on the order of 10^5 h. Therefore, whole detector imaging is the only appropriate technique based on the results of this model. This means the images obtained would be flashes, useful for showing changes in emission, but not for resolving specific spatial elements of the plasma structures.

3.4 Sources of Underestimation and Background Sources

The emission rates estimated by this model are likely an underestimate of what could realistically be detected due to the exclusion of other in-system neutral particle sources (only Enceladus-sourced neutrals are considered here). While Enceladus is the dominant provider of neutral particles in the Saturnian system, hydrogen is also sourced to the outer magnetosphere from Titan (H. T. Smith & Richardson, 2021). Titan orbits within the outer magnetosphere at $\sim 20\ R_S$, which can be within the magnetosheath when high solar wind dynamic pressure compresses the magnetosphere (Wei et al., 2009). In this case, ejection of hydrogen from Titan would lead to higher soft X-ray emission in the magnetosheath, if only locally. Neutral density has been shown to have an important effect on emission, so Titan could potentially play a large part in soft X-ray emission. With an orbital period of 16 days, much greater than the integration times reported in all cases discussed, Titan could potentially be followed throughout the magnetosheath by looking for local enhancements in emission along the orbital path of the moon. Additionally, Titan has no intrinsic magnetic field, so directly interacts with its plasma environment and generates an induced magnetosphere (N. F. Ness et al., 1982). When Titan is located within the magnetosheath, soft X-ray imaging may show signatures of the induced magnetosphere, with a cavity beyond the induced magnetopause where magnetosheath plasma is deflected and emission inhibited. Furthermore, if the magnetopause model was to include cusps (e.g. M. F. Smith and Lockwood (1996); Jasinski et al. (2016)), allowing entry of the solar wind deep into the magnetosphere, then hydrogen from Saturn's exosphere would start to make a non-negligible contribution towards X-ray generation.

Energetic Neutral Atoms (ENAs) also populate Saturn's magnetosphere, also produced through charge exchange processes (e.g. Kinrade et al. (2021)). A combination of soft X-ray and ENA imaging techniques could be used to build a full spatial picture

of the extended distribution of neutrals. Furthermore, if ENAs are present in the magnetosheath, their high velocities may drive localised hotspots in soft X-ray emission.

Cascades of charge exchange reactions through secondary interactions between neutrals and ions could potentially facilitate an increased X-ray emission rate. For example, once charge exchange has occurred between O^{7+} and a neutral, the product is O^{6+} (and an ionised neutral). This can charge exchange and will further lead to soft X-ray emission. Other ions than oxygen can also lead to soft X-ray emission (Bodewits et al., 2007). Naylor et al. (n.d.) made a simple comparison between considering only O^{7+} and the full range of solar wind ions by using the ACX (Atomic Charge Exchange, Smith et al. (2012)) model (`http://www.atomdb.org/CX/`). Using the ACX model, emission rates may be up to $\sim$ 3.5-4 times higher when a full solar wind range of ions is considered. Naylor et al. (n.d.) consider only O^{7+} charge exchange while this study considers both O^{7+} and O^{8+}, but the contribution from O^{8+} is relative small so the approximation of a $\sim$ 3.5-4$\times$ increase in emission is still valid.

There are many background sources of soft X-rays that must be considered alongside magnetosheath-sourced emission. These include the Sun (see review by Sibeck et al. (2018)), the heliopause (Cravens, 2000), Galactic sources (Snowden et al., 1990), the diffuse soft X-ray background (Giacconi et al., 1962; Snowden et al., 1997; McCammon et al., 2002), and other solar system charge exchange sites (e.g., the Jovian X-ray aurora, (Metzger et al., 1983; Cravens et al., 1995b, 2003)). Some of these are difficult to distinguish from one another (Yoshino et al., 2009) — for example, solar wind charge exchange (SWCX) emission within the heliosphere (Cravens, 2000; Lallement, R., 2004) and thermal emission from hot gas in the Local Bubble (McCammon & Sanders, 1990). Sibeck et al. (2018) showed that even after background subtraction, the terrestrial magnetosheath remains visible in soft X-rays. Kuntz and Snowden (2000) describe the soft X-ray diffuse background as being concentrated around 0.25 keV. Since this study focuses only on O^{7+} and O^{8+} charge exchange, which emits primarily between 0.5–1 keV, the diffuse background is not expected to be a significant contaminant. Galactic point sources, though more variable and therefore harder to remove from images, are significantly fainter. Other background sources, however, may still contribute and should be addressed in more detail in a future study.

Sibeck et al. (2018) demonstrated with a simple calculation that soft X-ray emission from Earth's magnetosheath should be readily distinguishable from the background. To compare Saturn's magnetosheath with Earth's, we follow their table 6, which estimates $R_{MP} \times n_q \times n_n \times v_{\rm rel}$ normalized to Earth, enabling comparison across planetary magnetosheaths. Adopting $R_{MP} \sim 20\ R_S$, $n_q \sim 0.1$ cm^{-3}, $n_n \sim 100$ cm^{-3}, and $v_{\rm rel} \sim 400$ km s^{-1} for Saturn gives a value of $\sim$1.2 relative to Earth. This suggests that Saturn's magnetosheath emission could be of comparable strength and thus be detectable above the background.

Overall, a full consideration of system physics and charge exchange would only serve to increase the possibilities of soft X-ray imaging of Saturn's magnetosheath. Background sources must be fully considered in order to ascertain whether the magnetosheath or cusps could be distinguished from heliospheric and galactic sources, for example. A future mission may consider that there are many potential objectives that an X-ray imager could strive to fulfil, including investigation of moon and ring fluorescence, potential auroral and planetary atmospheric imaging, characterisation of Titan's atmospheric loss to the solar wind and more.

3.5 Long Distance Imaging

Further approach distances are also investigated using a point source approximation. If an SXI is on board a dedicated mission to Saturn, then full imaging at a close approach distance will be the best method. However, if an SXI was attached to a mis-

sion en-route to another planet, the planned Uranus orbiter, for example, it is worth considering whether soft X-ray emission could be detected during its flight. While the point source approximation's validity is questionable at small distances, it is more justifiable at the large distance the spacecraft would be at during flight to another system. Figure 4 shows that even up to $\sim$ 8500 R_S $\sim$ 3.5 au, integration times for both the SMILE and future SXIs remain under the planetary rotation period (10.7 hours) and could detect Saturn's soft X-ray emission. While the detected flux would not give any insight into the magnetosheath due to being from a point, there are still investigations that could be performed using the rate of soft X-ray detection, for example count rate variability with rotation, solar wind conditions or Titan's location. That said, at the furthest distances shown in figure 4, out to 3.5 au, the spacecraft may be closer to other solar system bodies, so the orbital location of different bodies and contamination of results must be considered. Furthermore, smaller solar system bodies, for example, comets, should be considered during the whole approach stage. If there is a comet transiting Saturn and the spacecraft during approach, the emission from the comet (see Lisse et al. (1996)) may dominate over Saturn's emission. While this is an unlikely case, it highlights that Saturn is far from the only soft X-ray source in the solar system and contamination of flux must be considered. More likely, Titan's solar wind charge exchange would contaminate the results in a similar way. Spacecraft trajectories to avoid as many contaminating sources as possible should be considered, and if it not possible to do this, the SXI may be best being turned on later in its approach to the Saturnian system. As expected, figure 4 shows the integration times are much lower for the future SXI, but they are still reasonable for SMILE, reflecting that the drastic improvements suggested in the future SXI are likely not required for effective imaging of the Saturnian system.

Figure 4(b) shows the point source approximation extended back to an Earth orbit, to consider whether Saturn's soft X-ray emission may be visible to an Earth-orbiting observatory such as XMM-Newton. Effective areas of 4500 cm^2 and, more realistically due to needing to use certain optical filters, 2000 cm^2 are used to test what XMM-Newton may see. For a_{eff} = 2000 cm^2, XMM-Newton would detect X-rays from Saturn in $\sim$ 0.25 h, similar to the baseline conditions with the SMILE-like SXI. This corresponds to 10 photons detected within a quarter of a planetary rotation. When considering that emission is likely higher than what has been calculated here due to only oxygen charge exchange being considered, it could be expected that 35-40 photons may be detected within this quarter of a rotation timescale with a full range of solar wind ion consideration. This opens the possibility of Earth-based observations.

4 Conclusions

Soft X-ray emissions are generated within planetary magnetosheaths due to charge exchange interactions between highly charged solar wind ions, such as O^{7+} and O^{8+}, and magnetospheric neutral particles. They can be imaged to build a dynamic and global diagnostic of the magnetosheath and cusp regions and explore the driving of planetary magnetospheres by the solar wind (Sibeck et al., 2018). Saturn has a vast, neutral-dominated magnetosphere where the icy moon Enceladus sources water-group neutrals which spread across the system into the magnetosheath. This study presents a simple model of Saturn's magnetopause and bow shock to estimate soft X-ray emission rates generated within the magnetosheath. The magnetopause and bow shock are from the models of Kanani et al. (2010) and Went et al. (2011) respectively. Solar wind conditions are varied to investigate the driving of the emission by the solar wind, with speed, dynamic pressure and composition of the impinging solar wind altered. Three cases are imposed: slow solar wind, with a speed v_{SW} = 400 km s^{-1}, fast wind, with a speed v_{SW} = 650 km s^{-1}, and a sample from Thomsen et al. (2019), which uses Zieger and Hansen (2008)'s mSWIM solar wind propagation model. A simple analysis of imaging possibilities by a soft X-ray imager (SXI) are performed. The main results of the model include:

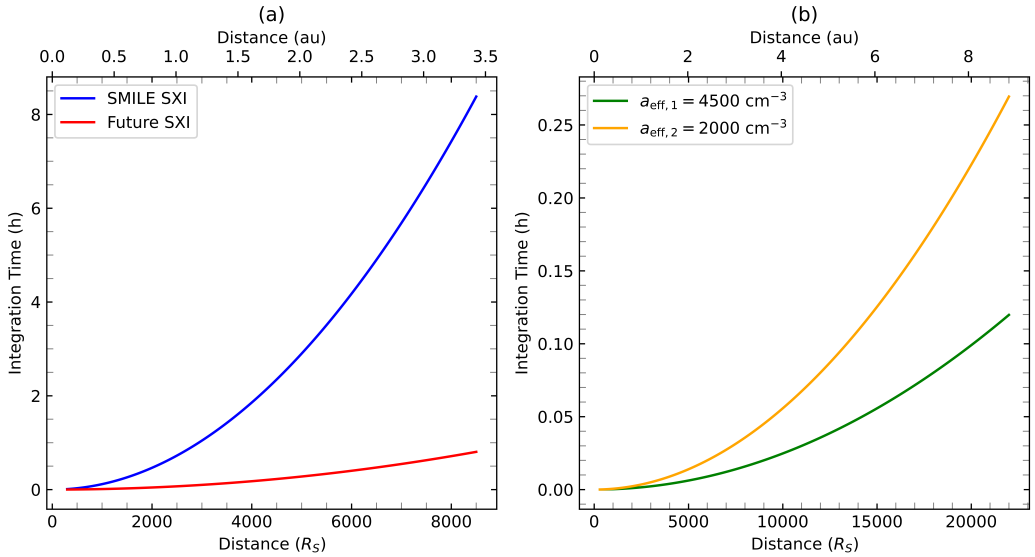

Figure 4. (a) Integration time in hours as a function of distance in R_S and au for both the SMILE (blue) and future (red) SXIs, with the Saturnian system acting as a point source, i.e. flux arriving from one point. Integration times for both detectors remain under one hour out to very large distances. (b) Integration times extending to Earth's distance from Saturn, with XMM-Newton-like detectors simulated with effective areas of 4500 cm^2 and 2000 cm^2.

1. Imaging the whole magnetosheath under slow solar wind conditions with a SMILE-like SXI at a distance of 260 R_S obtains volumetric emission rates on the order of 10^{-11} photon cm^{-3} s^{-1} and integration times around 15 minutes, too long for imaging to likely be viable.
2. Improvements to the SXI, including moving the SMILE-like detector closer and considering a future imager, with double the FOV of SMILE and an effective area of 100 cm^{-2}, much improve imaging viability and estimate that hundreds to thousands of photons could be imaged within a quarter of a planetary rotation.
3. Solar wind variations affect X-ray emission rates, with emission being on the order of 10^{-10} photon cm^{-3} s^{-1} for fast solar wind, significantly higher than slow wind, due to the higher relative speeds and the compression of the magnetosphere causing more neutrals to exist within the magnetosheath. For another sample where solar wind dynamic pressure is low, emission rates are significantly lower.
4. Under a point source approximation, both SXIs perform well, with integration times below the planetary rotation period even to distances of 8500 R_S = 3.5 au. Extending the point source approximation to Earth shows that observations of Saturn's magnetosheath with an XMM-Newton-like detector may be possible.

Emission rates calculated in this model are likely an underestimate for various reasons, including the non-inclusion of magnetospheric cusps, the contribution of Titan to the neutral environment, and only considering highly-charged oxygen solar wind charge exchange. With the full range of solar wind ions, we anticipate that X-ray emission rates could be up to 4 times higher. Overall, this study reveals that X-ray investigations at Saturn could reveal more about the magnetosheath and cusp regions as well as the near-Titan environment and improve understanding of the solar wind driving of the magnetosphere. Current X-ray imaging technology is likely sufficient to investigate the system although im-

provements to detector FOV and effective area could allow for imaging of rapid changes to the magnetosheath.

Acronyms

SXI Soft X-Ray Imager
SMILE Solar wind-Magnetosphere-Ionosphere Link Explorer
FOV Field-of-View
ENA Energetic Neutral Atom
MHD Magnetohydrodynamic
KSM Kronocentric Solar Magnetospheric
ACX Atomic Charge Exchange

Conflict of Interest Statement

The authors have no conflicts of interest to disclose.

Open Research Section

Model output files are available at Naylor et al. (2025).

Acknowledgments

D.N. was supported by an STFC Studentship to Lancaster University. L.C.R. was supported by STFC Grant ST/Y002148/1 to Lancaster University. Primary research of P.C.R. was conducted at Lancaster University; further work completed while at University of Cologne. W.R.D. is supported by an STFC Ernest Rutherford Fellowship: ST/W003449/1.

References

Bhardwaj, A., Elsner, R. F., Waite, J. H., Jr., Gladstone, G. R., Cravens, T. E., & Ford, P. G. (2005, apr). Chandra observation of an x-ray flare at saturn: Evidence of direct solar control on saturn's disk x-ray emissions. *The Astrophysical Journal*, *624*(2), L121. Retrieved from `https://dx.doi.org/10.1086/430521` doi: 10.1086/430521

Bodewits, D., Christian, D. J., Torney, M., Dryer, M., Lisse, C. M., Dennerl, K., ... Hoekstra, R. (2007). Spectral analysis of the chandra comet survey*. *A&A*, *469*(3), 1183-1195. Retrieved from `https://doi.org/10.1051/0004-6361:20077410` doi: 10.1051/0004-6361:20077410

Branduardi-Raymont, G., Bhardwaj, A., Elsner, R. F., & Rodriguez, P. (2010). X-rays from saturn: a study with xmm-newton and chandra over the years 2002–05. *A&A*, *510*, A73. Retrieved from `https://doi.org/10.1051/0004-6361/200913110` doi: 10.1051/0004-6361/200913110

Branduardi-Raymont, G., Ford, P. G., Hansen, K. C., Lamy, L., Masters, A., Cecconi, B., ... Zarka, P. (2013). Search for saturn's x-ray aurorae at the arrival of a solar wind shock. *Journal of Geophysical Research: Space Physics*, *118*(5), 2145-2156. Retrieved from `https://agupubs.onlinelibrary.wiley.com/doi/abs/10.1002/jgra.50112` doi: https://doi.org/10.1002/jgra.50112

Bunce, E. J., Cowley, S. W. H., Wright, D. M., Coates, A. J., Dougherty, M. K., Krupp, N., ... Rymer, A. M. (2005). In situ observations of a solar wind compression-induced hot plasma injection in saturn's tail. *Geophysical Research Letters*, *32*(20). Retrieved from `https://agupubs.onlinelibrary.wiley.com/doi/abs/10.1029/2005GL022888` doi: https://doi.org/10.1029/2005GL022888

Connor, H. K., Sibeck, D. G., Collier, M. R., Baliukin, I. I., Branduardi-Raymont, G., Brandt, P. C., ... Zoennchen, J. H. (2021). Soft x-ray and ena imaging of the earth's dayside magnetosphere. *Journal of Geophysical Research: Space Physics*, *126*(3), e2020JA028816. Retrieved from https://agupubs.onlinelibrary.wiley.com/doi/abs/10.1029/2020JA028816 (e2020JA028816 2020JA028816) doi: https://doi.org/10.1029/2020JA028816

Cravens, T. E. (2000, mar). Heliospheric x-ray emission associated with charge transfer of the solar wind with interstellar neutrals. *The Astrophysical Journal*, *532*(2), L153. Retrieved from https://dx.doi.org/10.1086/312574 doi: 10.1086/312574

Cravens, T. E., Clark, J., Bhardwaj, A., Elsner, R., Waite Jr., J. H., Maurellis, A. N., ... Branduardi-Raymont, G. (2006). X-ray emission from the outer planets: Albedo for scattering and fluorescence of solar x rays. *Journal of Geophysical Research: Space Physics*, *111*(A7). Retrieved from https://agupubs.onlinelibrary.wiley.com/doi/abs/10.1029/2005JA011413 doi: https://doi.org/10.1029/2005JA011413

Cravens, T. E., Howell, E., Waite Jr., J. H., & Gladstone, G. R. (1995a). Auroral oxygen precipitation at jupiter. *Journal of Geophysical Research: Space Physics*, *100*(A9), 17153-17161. Retrieved from https://agupubs.onlinelibrary.wiley.com/doi/abs/10.1029/95JA00970 doi: https://doi.org/10.1029/95JA00970

Cravens, T. E., Howell, E., Waite Jr., J. H., & Gladstone, G. R. (1995b). Auroral oxygen precipitation at jupiter. *Journal of Geophysical Research: Space Physics*, *100*(A9), 17153-17161. Retrieved from https://agupubs.onlinelibrary.wiley.com/doi/abs/10.1029/95JA00970 doi: https://doi.org/10.1029/95JA00970

Cravens, T. E., Waite, J. H., Gombosi, T. I., Lugaz, N., Gladstone, G. R., Mauk, B. H., & MacDowall, R. J. (2003). Implications of jovian x-ray emission for magnetosphere-ionosphere coupling. *Journal of Geophysical Research: Space Physics*, *108*(A12). Retrieved from https://agupubs.onlinelibrary.wiley.com/doi/abs/10.1029/2003JA010050 doi: https://doi.org/10.1029/2003JA010050

Dunn, W. R., Weigt, D. M., Grodent, D., Yao, Z. H., May, D., Feigelman, K., ... Ray, L. C. (2022). Jupiter's x-ray and uv dark polar region. *Geophysical Research Letters*, *49*(11), e2021GL097390. Retrieved from https://agupubs.onlinelibrary.wiley.com/doi/abs/10.1029/2021GL097390 (e2021GL097390 2021GL097390) doi: https://doi.org/10.1029/2021GL097390

Esposito, L. W., Colwell, J. E., Larsen, K., McClintock, W. E., Stewart, A. I. F., Hallett, J. T., ... Yung, Y. L. (2005). Ultraviolet imaging spectroscopy shows an active saturnian system. *Science*, *307*(5713), 1251-1255. Retrieved from https://www.science.org/doi/abs/10.1126/science.1105606 doi: 10.1126/science.1105606

Fraser, G., Carpenter, J., Rothery, D., Pearson, J., Martindale, A., Huovelin, J., ... Whitehead, S. (2010). The mercury imaging x-ray spectrometer (mixs) on bepicolombo. *Planetary and Space Science*, *58*(1), 79-95. Retrieved from https://www.sciencedirect.com/science/article/pii/S0032063309001482 (Comprehensive Science Investigations of Mercury: The scientific goals of the joint ESA/JAXA mission BepiColombo) doi: https://doi.org/10.1016/j.pss.2009.05.004

Fuselier, S. A., Petrinec, S. M., Sawyer, R. P., Mukherjee, J., & Masters, A. (2020). Suppression of magnetic reconnection at saturn's low-latitude magnetopause. *Journal of Geophysical Research: Space Physics*, *125*(5), e2020JA027895. Retrieved from https://agupubs.onlinelibrary.wiley.com/doi/abs/10.1029/2020JA027895 (e2020JA027895 2020JA027895) doi: https://doi.org/10.1029/2020JA027895

Giacconi, R., Gursky, H., Paolini, F. R., & Rossi, B. B. (1962, Dec). Evidence for x rays from sources outside the solar system. *Phys. Rev. Lett.*, *9*, 439–443. Retrieved from https://link.aps.org/doi/10.1103/PhysRevLett.9.439 doi: 10.1103/PhysRevLett.9.439

Gustin, J., Bonfond, B., Grodent, D., & Gérard, J.-C. (2012). Conversion from hst acs and stis auroral counts into brightness, precipitated power, and radiated power for h2 giant planets. *Journal of Geophysical Research: Space Physics*, *117*(A7). Retrieved from https://agupubs.onlinelibrary.wiley.com/doi/abs/10.1029/2012JA017607 doi: https://doi.org/10.1029/2012JA017607

Huddleston, D. E., Russell, C. T., Le, G., & Szabo, A. (1997). Magnetopause structure and the role of reconnection at the outer planets. *Journal of Geophysical Research: Space Physics*, *102*(A11), 24289-24302. Retrieved from https://agupubs.onlinelibrary.wiley.com/doi/abs/10.1029/97JA02416 doi: https://doi.org/10.1029/97JA02416

Hui, Y., Cravens, T. E., Ozak, N., & Schultz, D. R. (2010). What can be learned from the absence of auroral x-ray emission from saturn? *Journal of Geophysical Research: Space Physics*, *115*(A10). Retrieved from https://agupubs.onlinelibrary.wiley.com/doi/abs/10.1029/2010JA015639 doi: https://doi.org/10.1029/2010JA015639

Jackman, C. M., Thomsen, M. F., & Dougherty, M. K. (2019). Survey of saturn's magnetopause and bow shock positions over the entire cassini mission: Boundary statistical properties and exploration of associated upstream conditions. *Journal of Geophysical Research: Space Physics*, *124*(11), 8865-8883. Retrieved from https://agupubs.onlinelibrary.wiley.com/doi/abs/10.1029/2019JA026628 doi: https://doi.org/10.1029/2019JA026628

Jasinski, J. M., Arridge, C. S., Coates, A. J., Jones, G. H., Sergis, N., Thomsen, M. F., ... Waite Jr., J. H. (2016). Cassini plasma observations of saturn's magnetospheric cusp. *Journal of Geophysical Research: Space Physics*, *121*(12), 12,047-12,067. Retrieved from https://agupubs.onlinelibrary.wiley.com/doi/abs/10.1002/2016JA023310 doi: https://doi.org/10.1002/2016JA023310

Jia, X., Hansen, K. C., Gombosi, T. I., Kivelson, M. G., Tóth, G., DeZeeuw, D. L., & Ridley, A. J. (2012). Magnetospheric configuration and dynamics of saturn's magnetosphere: A global mhd simulation. *Journal of Geophysical Research: Space Physics*, *117*(A5). Retrieved from https://agupubs.onlinelibrary.wiley.com/doi/abs/10.1029/2012JA017575 doi: https://doi.org/10.1029/2012JA017575

Johnson, R., Luhmann, J., Tokar, R., Bouhram, M., Berthelier, J., Sittler, E., ... Young, D. (2006). Production, ionization and redistribution of o2 in saturn's ring atmosphere. *Icarus*, *180*(2), 393-402. Retrieved from https://www.sciencedirect.com/science/article/pii/S001910350500326X doi: https://doi.org/10.1016/j.icarus.2005.08.021

Jurac, S., & Richardson, J. D. (2005). A self-consistent model of plasma and neutrals at saturn: Neutral cloud morphology. *Journal of Geophysical Research: Space Physics*, *110*(A9). Retrieved from https://agupubs.onlinelibrary.wiley.com/doi/abs/10.1029/2004JA010635 doi: https://doi.org/10.1029/2004JA010635

Kanani, S. J., Arridge, C. S., Jones, G. H., Fazakerley, A. N., McAndrews, H. J., Sergis, N., ... Krupp, N. (2010). A new form of saturn's magnetopause using a dynamic pressure balance model, based on in situ, multi-instrument cassini measurements. *Journal of Geophysical Research: Space Physics*, *115*(A6). Retrieved from https://agupubs.onlinelibrary.wiley.com/doi/abs/10.1029/2009JA014262 doi: https://doi.org/10.1029/2009JA014262

Kinrade, J., Bader, A., Badman, S. V., Paranicas, C., Mitchell, D. G., Constable, D., ... Provan, G. (2021). The statistical morphology of saturn's equato-

rial energetic neutral atom emission. *Geophysical Research Letters*, *48*(11), e2020GL091595. Retrieved from https://agupubs.onlinelibrary.wiley.com/doi/abs/10.1029/2020GL091595 (e2020GL091595 2020GL091595) doi: https://doi.org/10.1029/2020GL091595

Kuntz, K. D., & Snowden, S. L. (2000, nov). Deconstructing the spectrum of the soft x-ray background. *The Astrophysical Journal*, *543*(1), 195. Retrieved from https://dx.doi.org/10.1086/317071 doi: 10.1086/317071

Lallement, R. (2004). The heliospheric soft x-ray emission pattern during the rosat survey: Inferences on local bubble hot gas. *A&A*, *418*(1), 143-150. Retrieved from https://doi.org/10.1051/0004-6361:20040059 doi: 10.1051/0004-6361:20040059

Leppard, F., Patrick, A., Ray, L., Dunn, W. R., Smith, H. T., Yao, Z., ... Wang, C. (2025). Estimating solar wind charge exchange generated soft x-rays in the jovian magnetosheath. *Journal of Geophysical Research: Space Physics*, *130*(7), e2024JA033415. Retrieved from https://agupubs.onlinelibrary.wiley.com/doi/abs/10.1029/2024JA033415 (e2024JA033415 2024JA033415) doi: https://doi.org/10.1029/2024JA033415

Lisse, C. M., Dennerl, K., Englhauser, J., Harden, M., Marshall, F. E., Mumma, M. J., ... West, R. G. (1996). Discovery of x-ray and extreme ultraviolet emission from comet c/hyakutake 1996 b2. *Science*, *274*(5285), 205-209. Retrieved from https://www.science.org/doi/abs/10.1126/science.274.5285.205 doi: 10.1126/science.274.5285.205

Masters, A., Fujimoto, M., Hasegawa, H., Russell, C. T., Coates, A. J., & Dougherty, M. K. (2014). Can magnetopause reconnection drive saturn's magnetosphere? *Geophysical Research Letters*, *41*(6), 1862-1868. Retrieved from https://agupubs.onlinelibrary.wiley.com/doi/abs/10.1002/2014GL059288 doi: https://doi.org/10.1002/2014GL059288

McCammon, D., Almy, R., Apodaca, E., Bergmann Tiest, W., Cui, W., Deiker, S., ... Szymkowiak, A. E. (2002, sep). A high spectral resolution observation of the soft x-ray diffuse background with thermal detectors. *The Astrophysical Journal*, *576*(1), 188. Retrieved from https://dx.doi.org/10.1086/341727 doi: 10.1086/341727

McCammon, D., & Sanders, W. T. (1990). The soft x-ray background and its origins [Journal Article]. *Annual Review of Astronomy and Astrophysics*, *28*(Volume 28, 1990), 657-688. Retrieved from https://www.annualreviews.org/content/journals/10.1146/annurev.aa.28.090190.003301 doi: https://doi.org/10.1146/annurev.aa.28.090190.003301

Melin, H., Shemansky, D. E., & Liu, X. (2009). The distribution of atomic hydrogen and oxygen in the magnetosphere of saturn. *Planetary and Space Science*, *57*(14), 1743-1753. Retrieved from https://www.sciencedirect.com/science/article/pii/S0032063309001275 doi: https://doi.org/10.1016/j.pss.2009.04.014

Metzger, A. E., Gilman, D. A., Luthey, J. L., Hurley, K. C., Schnopper, H. W., Seward, F. D., & Sullivan, J. D. (1983). The detection of x rays from jupiter. *Journal of Geophysical Research: Space Physics*, *88*(A10), 7731-7741. Retrieved from https://agupubs.onlinelibrary.wiley.com/doi/abs/10.1029/JA088iA10p07731 doi: https://doi.org/10.1029/JA088iA10p07731

Mo, W., Vines, S. K., Allen, R. C., Jackman, C. M., & Paranicas, C. (2023). Magnetopause dynamics at saturn as observed by cassini. *Journal of Geophysical Research: Space Physics*, *128*(8), e2022JA031258. Retrieved from https://agupubs.onlinelibrary.wiley.com/doi/abs/10.1029/2022JA031258 (e2022JA031258 2022JA031258) doi: https://doi.org/10.1029/2022JA031258

Naylor, D., Ray, L. C., Dunn, W. R., Jasinski, J. M., & Paty, C. (n.d.). Estimating soft x-ray emission from uranus's magnetosheath. *Journal of Geophysical Research: Space Physics*.

Naylor, D., Ray, L. C., Dunn, W. R., & Smith, H. T. (2025). *Model outputs: Soft x-ray emission from saturn's magnetosheath ii: Solar wind driving.* https://doi.org/10.17635/lancaster/researchdata/728. (Lancaster University)

Ness, J.-U., Schmitt, J. H. M. M., & Robrade, J. (2004). Detection of saturnian x-ray emission with xmm-newton. *A&A*, *414*(3), L49-L52. Retrieved from https://doi.org/10.1051/0004-6361:20031761 doi: 10.1051/0004-6361:20031761

Ness, J.-U., Schmitt, J. H. M. M., Wolk, S. J., Dennerl, K., & Burwitz, V. (2004). X-ray emission from saturn. *A&A*, *418*(1), 337-345. Retrieved from https://doi.org/10.1051/0004-6361:20035736 doi: 10.1051/0004-6361:20035736

Ness, N. F., Acuna, M. H., Behannon, K. W., & Neubauer, F. M. (1982). The induced magnetosphere of titan. *Journal of Geophysical Research: Space Physics*, *87*(A3), 1369-1381. Retrieved from https://agupubs.onlinelibrary.wiley.com/doi/abs/10.1029/JA087iA03p01369 doi: https://doi.org/10.1029/JA087iA03p01369

Ng, J., Walsh, B. M., Chen, L.-J., & Omelchenko, Y. (2023). Soft x-ray imaging of earth's dayside magnetosheath and cusps using hybrid simulations. *Geophysical Research Letters*, *50*(10), e2023GL103347. Retrieved from https://agupubs.onlinelibrary.wiley.com/doi/abs/10.1029/2023GL103347 (e2023GL103347 2023GL103347) doi: https://doi.org/10.1029/2023GL103347

Nitti, S., Carter, J. A., Sembay, S. F., Milan, S. E., Zhao, L., Lepri, S. T., & Kuntz, K. D. (2024). Can xmm-newton be used to track compositional changes in the solar wind? *Journal of Geophysical Research: Space Physics*, *129*(12), e2024JA033323. Retrieved from https://agupubs.onlinelibrary.wiley.com/doi/abs/10.1029/2024JA033323 (e2024JA033323 2024JA033323) doi: https://doi.org/10.1029/2024JA033323

Pilkington, N. M., Achilleos, N., Arridge, C. S., Guio, P., Masters, A., Ray, L. C., ... Dougherty, M. K. (2015). Internally driven large-scale changes in the size of saturn's magnetosphere. *Journal of Geophysical Research: Space Physics*, *120*(9), 7289-7306. Retrieved from https://agupubs.onlinelibrary.wiley.com/doi/abs/10.1002/2015JA021290 doi: https://doi.org/10.1002/2015JA021290

Pilkington, N. M., Achilleos, N., Arridge, C. S., Masters, A., Sergis, N., Coates, A. J., & Dougherty, M. K. (2014). Polar confinement of saturn's magnetosphere revealed by in situ cassini observations. *Journal of Geophysical Research: Space Physics*, *119*(4), 2858-2875. Retrieved from https://agupubs.onlinelibrary.wiley.com/doi/abs/10.1002/2014JA019774 doi: https://doi.org/10.1002/2014JA019774

Porco, C. C., Helfenstein, P., Thomas, P. C., Ingersoll, A. P., Wisdom, J., West, R., ... Squyres, S. (2006). Cassini observes the active south pole of enceladus. *Science*, *311*(5766), 1393-1401. Retrieved from https://www.science.org/doi/abs/10.1126/science.1123013 doi: 10.1126/science.1123013

Richardson, J. D., Eviatar, A., McGrath, M. A., & Vasyliũnas, V. M. (1998). Oh in saturn's magnetosphere: Observations and implications. *Journal of Geophysical Research: Planets*, *103*(E9), 20245-20255. Retrieved from https://agupubs.onlinelibrary.wiley.com/doi/abs/10.1029/98JE01127 doi: https://doi.org/10.1029/98JE01127

Rogan, P. C., Ray, L. C., Naylor, D., Dunn, W. R., Jia, X., Smith, H. T., & Sulaiman, A. (submitted). Soft x-ray emission from saturn's magnetosheath i: 3d modelling from mhd data. *Journal of Geophysical Research: Space Physics*.

Schwadron, N. A., & Cravens, T. E. (2000, nov). Implications of solar wind composition for cometary x-rays. *The Astrophysical Journal*, *544*(1), 558. Retrieved from https://dx.doi.org/10.1086/317176 doi: 10.1086/317176

Sembay, S., Alme, A. L., Agnolon, D., Arnold, T., Beardmore, A., Margeli, A. B. B., ... Yang, S. (2024). The soft x-ray imager (sxi) on the smile mission. *Earth*

and Planetary Physics, *8*(1), 5-14. Retrieved from https://www.eppcgs.org/en/article/doi/10.26464/epp2023067 doi: 10.26464/epp2023067

Sergis, N., Jackman, C. M., Masters, A., Krimigis, S. M., Thomsen, M. F., Hamilton, D. C., ... Coates, A. J. (2013). Particle and magnetic field properties of the saturnian magnetosheath: Presence and upstream escape of hot magnetospheric plasma. *Journal of Geophysical Research: Space Physics*, *118*(4), 1620-1634. Retrieved from https://agupubs.onlinelibrary.wiley.com/doi/abs/10.1002/jgra.50164 doi: https://doi.org/10.1002/jgra.50164

Shemansky, D. E., & Hall, D. T. (1992). The distribution of atomic hydrogen in the magnetosphere of saturn. *Journal of Geophysical Research: Space Physics*, *97*(A4), 4143-4161. Retrieved from https://agupubs.onlinelibrary.wiley.com/doi/abs/10.1029/91JA02805 doi: https://doi.org/10.1029/91JA02805

Shemansky, D. E., Matheson, P., Hall, D. T., Hu, H.-Y., & Tripp, T. M. (1993). Detection of the hydroxyl radical in the saturn magnetosphere. *Nature (London)*, *363*(6427), 329-331.

Shen, C., Ren, N., Qureshi, M. N. S., & Guo, Y. (2022). On the temperatures of planetary magnetosheaths at the subsolar points. *Journal of Geophysical Research: Space Physics*, *127*(11), e2022JA030782. Retrieved from https://agupubs.onlinelibrary.wiley.com/doi/abs/10.1029/2022JA030782 (e2022JA030782 2022JA030782) doi: https://doi.org/10.1029/2022JA030782

Sibeck, D. G., Allen, R., Aryan, H., Bodewits, D., Brandt, P., Branduardi-Raymont, G., ... Wing, S. (2018, June). Imaging Plasma Density Structures in the Soft X-Rays Generated by Solar Wind Charge Exchange with Neutrals. *ssr*, *214*(4), 79. doi: 10.1007/s11214-018-0504-7

Smith, H. T., & Richardson, J. D. (2021). The 3d structure of saturn magnetospheric neutral tori produced by the enceladus plumes. *Journal of Geophysical Research: Space Physics*, *126*(3), e2020JA028775. Retrieved from https://agupubs.onlinelibrary.wiley.com/doi/abs/10.1029/2020JA028775 (e2020JA028775 2020JA028775) doi: https://doi.org/10.1029/2020JA028775

Smith, M. F., & Lockwood, M. (1996). Earth's magnetospheric cusps. *Reviews of Geophysics*, *34*(2), 233-260. Retrieved from https://agupubs.onlinelibrary.wiley.com/doi/abs/10.1029/96RG00893 doi: https://doi.org/10.1029/96RG00893

Smith, R. K., Foster, A. R., & Brickhouse, N. S. (2012, April). Approximating the X-ray spectrum emitted from astrophysical charge exchange. *Astronomische Nachrichten*, *333*(4), 301. doi: 10.1002/asna.201211673

Snowden, S. L., Cox, D. P., McCammon, D., & Sanders, W. T. (1990, May). A Model for the Distribution of Material Generating the Soft X-Ray Background. *The Astrophysical Journal*, *354*, 211. doi: 10.1086/168680

Snowden, S. L., Egger, R., Freyberg, M. J., McCammon, D., Plucinsky, P. P., Sanders, W. T., ... Voges, W. (1997, aug). Rosat survey diffuse x-ray background maps. ii. *The Astrophysical Journal*, *485*(1), 125. Retrieved from https://dx.doi.org/10.1086/304399 doi: 10.1086/304399

Spencer, J. R., Pearl, J. C., Segura, M., Flasar, F. M., Mamoutkine, A., Romani, P., ... Lopes, R. M. C. (2006). Cassini encounters enceladus: Background and the discovery of a south polar hot spot. *Science*, *311*(5766), 1401-1405. Retrieved from https://www.science.org/doi/abs/10.1126/science.1121661 doi: 10.1126/science.1121661

Thomsen, M. F., Jackman, C. M., & Lamy, L. (2019). Solar wind dynamic pressure upstream from saturn: Estimation from magnetosheath properties and comparison with skr. *Journal of Geophysical Research: Space Physics*, *124*(10), 7799-7819. Retrieved from https://agupubs.onlinelibrary.wiley.com/doi/abs/10.1029/2019JA026819 doi: https://doi.org/10.1029/2019JA026819

Walsh, B. M., Kuntz, K. D., Busk, S., Cameron, T., Chornay, D., Chuchra, A., ...

Winkert, G. (2024, May). The Lunar Environment Heliophysics X-ray Imager (LEXI) Mission. *ssr*, *220*(4), 37. doi: 10.1007/s11214-024-01063-4

Wei, H. Y., Russell, C. T., Wellbrock, A., Dougherty, M. K., & Coates, A. J. (2009). Plasma environment at titan's orbit with titan present and absent. *Geophysical Research Letters*, *36*(23). Retrieved from https://agupubs.onlinelibrary.wiley.com/doi/abs/10.1029/2009GL041048 doi: https://doi.org/10.1029/2009GL041048

Weiser, H., Vitz, R. C., & Moos, H. W. (1977). Detection of lyman alpha emission from the saturnian disk and from the ring system. *Science*, *197*(4305), 755-757. Retrieved from https://www.science.org/doi/abs/10.1126/science.197.4305.755 doi: 10.1126/science.197.4305.755

Went, D. R., Hospodarsky, G. B., Masters, A., Hansen, K. C., & Dougherty, M. K. (2011). A new semiempirical model of saturn's bow shock based on propagated solar wind parameters. *Journal of Geophysical Research: Space Physics*, *116*(A7). Retrieved from https://agupubs.onlinelibrary.wiley.com/doi/abs/10.1029/2010JA016349 doi: https://doi.org/10.1029/2010JA016349

Whittaker, I. C., & Sembay, S. (2016). A comparison of empirical and experimental o7+, o8+, and o/h values, with applications to terrestrial solar wind charge exchange. *Geophysical Research Letters*, *43*(14), 7328-7337. Retrieved from https://agupubs.onlinelibrary.wiley.com/doi/abs/10.1002/2016GL069914 doi: https://doi.org/10.1002/2016GL069914

Whittaker, I. C., Sembay, S., Carter, J. A., Read, A. M., Milan, S. E., & Palmroth, M. (2016). Modeling the magnetospheric x-ray emission from solar wind charge exchange with verification from xmm-newton observations. *Journal of Geophysical Research: Space Physics*, *121*(5), 4158-4179. Retrieved from https://agupubs.onlinelibrary.wiley.com/doi/abs/10.1002/2015JA022292 doi: https://doi.org/10.1002/2015JA022292

Yoshino, T., Mitsuda, K., Yamasaki, N. Y., Takei, Y., Hagihara, T., Masui, K., ... Yao, Y. (2009, 08). Energy spectra of the soft x-ray diffuse emission in fourteen fields observed with suzaku. *Publications of the Astronomical Society of Japan*, *61*(4), 805-823. Retrieved from https://doi.org/10.1093/pasj/61.4.805 doi: 10.1093/pasj/61.4.805

Zieger, B., & Hansen, K. C. (2008). Statistical validation of a solar wind propagation model from 1 to 10 au. *Journal of Geophysical Research: Space Physics*, *113*(A8). Retrieved from https://agupubs.onlinelibrary.wiley.com/doi/abs/10.1029/2008JA013046 doi: https://doi.org/10.1029/2008JA013046